Local seismicity around the Chain Transform Fault at the Mid-Atlantic Ridge from OBS observations

David Schlaphorst[1,2]*, Catherine A. Rychert[3], Nicholas Harmon[3], Stephen P. Hicks[4], Petros Bogiatzis[3], J-Michael Kendall[5], Rachel E. Abercrombie[6]

(*corresponding author: dschlaphorst@fc.ul.pt)

[1] Instituto Dom Luiz (IDL), Faculdade de Ciências, Universidade de Lisboa, Campo Grande, 1749-016 Lisboa, Portugal.

[2] School of Earth Sciences, University of Bristol, Wills Memorial Building, Queens Road, Bristol BS8 1RJ, UK.

[3] Ocean and Earth Science, University of Southampton, National Oceanography Centre, Southampton, UK

[4] Department of Earth Science and Engineering, Imperial College London, UK.

[5] Department of Earth Sciences, University of Oxford, UK.

[6] Department of Earth & Environment, Boston University, USA.

Summary

Seismicity along transform faults provides important constraints for our understanding of the factors that control earthquake ruptures. Oceanic transform faults are particularly informative due to their relatively simple structure in comparison to their continental counterparts. The seismicity of several fast-moving transform faults has been investigated by local networks, but as of today there been few studies of transform faults in slow spreading ridges. Here we present the first local seismicity catalogue based on event data recorded by a temporary broadband network of 39 ocean bottom seismometers located around the slow-moving Chain Transform Fault (CTF) along the Mid-Atlantic Ridge (MAR) from March 2016 to March 2017. We locate 972 events in the area by simultaneously inverting for a 1-D velocity model informed by the event P- and S-arrival times. We refine the depths and focal mechanisms of the larger events using deviatoric moment tensor inversion. Most of the earthquakes are located along the CTF (700) and Romanche transform fault (94) and the MAR (155); a smaller number (23) can be observed on the continuing fracture zones or in intraplate locations. The ridge events are characterised by normal faulting and most of the transform events are characterised by strike slip faulting, but with several reverse mechanisms that are likely related to transpressional stresses in the region. CTF events range in magnitude from 1.1 to 5.6 with a magnitude of completeness around 2.3. Along the CTF we calculate a *b*-value of 0.81 ± 0.09. The event depths are mostly shallower than 15 km below sea level (523), but a small number of high-quality earthquakes (16) are located deeper, with some (8) located deeper than the brittle-ductile transition as predicted by the 600˚C-isotherm from a simple thermal model. The deeper events could be explained by the control of seawater infiltration on the brittle failure limit.

Keywords: Seismicity, Atlantic Ocean, Mid-ocean ridge processes, Oceanic transform and fracture zone processes, Seismicity and tectonics.

Introduction

The factors that dictate the location, size and style of earthquake faulting are fundamental to our understanding of hazard and hazard mitigation (e.g., Slemmons et al., 1986). Oceanic transform faults (OTF), such as those that connect the many fragmented sections of the slow spreading Mid-Atlantic Ridge, are an ideal place to investigate the earthquake cycle. While not a great risk to humans themselves due to their often remote locations, OTFs are thought to be relatively simple in terms of thermal structure, fault zone geometry, slip rate and rheology in comparison to more hazardous continental counterparts such as the San Andreas fault (Behn et al., 2007). Therefore, the study of earthquakes associated with OTFs provides important constraints to inform hazard assessments in continental areas. Ocean lithosphere is characterised by relatively homogenous composition, with mafic to ultra-mafic lithologies. In addition, deformation tends to be localised in a narrow zone, roughly 20 to 30 km wide (Fox & Gallo 1984) with nearly vertically oriented faults on which total motions should roughly correspond to ridge spreading rates. Finally, the region of potential seismic slip is also well-predicted by the region shallower than the 600˚C isotherm predicted by simple thermal models such as the halfspace cooling model (e.g., Abercrombie & Ekström, 2001).

The vast majority of earthquakes along OTFs cannot be detected, due to their general inaccessibility. Being in the middle of the ocean, the closest landmasses and, thus, seismic land stations are often located at teleseismic distances. Previous studies of Atlantic transform earthquakes have used teleseismic data (e.g., Engeln et al., 1986; Bergman & Solomon, 1988; Abercrombie & Ekström, 2001). Smaller events are not recorded teleseismically, and the magnitude of completeness offered by global monitoring networks is high, around 4.4 (Parnell-Turner et al., 2022). This affects the observation of microseismicity around the

70 brittle-ductile transition. Furthermore, the use of a non-local velocity model can influence the
71 accuracy of hypocentre depth localisations.
72
73 Over the last decade the temporary deployment of dense ocean bottom seismometer (OBS)
74 networks has enabled more detailed study of local seismicity along Pacific OTFs, e.g., along
75 the Gofar and Discovery OTFs (McGuirre et al., 2012) and the Blanco OTF (Kuna et al.,
76 2019). Spreading rates in the Pacific are mostly classified as intermediate or even fast (> 60
77 mm/yr), whereas the MAR is a slow-spreading ridge, which affects the rate and depth range,
78 and potentially other aspects of the local seismicity. The Chain and Romanche, as well as
79 other slow-slipping OTFs in the Atlantic, are likely variable in structure, potentially
80 containing areas of very thin crust and highly serpentinized mantle (Detrick et al., 1993;
81 Marjanovic et al., 2020; Gregory et al., 2021) and teleseismic earthquakes can be observed in
82 the shallow mantle beneath (Abercrombie & Ekström, 2001). While there have been studies
83 using OBS networks to investigate ridge segments or ridge-transform intersections in the
84 Atlantic (e.g., Toomey at al., 1985; Grevemeyer et al., 2013, Gregory et al., 2021; Yu et al.,
85 2021), local studies of Atlantic OTFs have been sparse.
86
87 From March 2016 to March 2017, a temporary network of 39 seismic ocean bottom
88 seismometers (OBS) was deployed around the Chain transform fault (CTF) on the MAR and
89 continuing eastward fracture zone (CFZ) as part of the PI-LAB ("Passive Imaging of the
90 Lithosphere-Asthenosphere Boundary") project and EURO-LAB (Experiment to Unearth the
91 Rheological Oceanic Lithosphere-Asthenosphere Boundary) (Fig. 1; Agius et al., 2018, 2021;
92 Harmon et al., 2018, 2020, 2021, 2022; Hicks et al., 2020; Bogiatzis et al., 2020; Wang et al.,
93 2019, 2020; Rychert et al., 2016, 2021; Saikia et al., 2020, 2021; Leptokaropoulos et al.,
94 2021, 2023). The CTF zone has a length of 300 km and varies in width between 7 km and 20

km with an African Plate half-spreading rate of 18.2mm/yr and a South American Plate half spreading rate of 15.7mm/yr (DeMets et al., 1994; Harmon et al., 2018). The aim of the experiment was to achieve a better understanding of the definition of the tectonic plate (Fischer et al., 2010, 2020; Rychert & Shearer, 2009; Rychert et al., 2005, 2007, 2010, 2018a 2018b, 2020; Tharimena et al., 2016, 2017a, 2017b). The deployment occurred on oceanic crust from its formation at the MAR to older plate ages away from the ridge; the setup was chosen to facilitate the observation of thickening oceanic lithosphere relative to increasing plate age. However, the experiment also offers an opportunity to study nearby plate boundary seismicity. During the same time, the International Seismic Centre (ISC) recorded 40 earthquakes in the region, of which 23 are located in the vicinity of the Romanche transform fault (RTF), 7 close to the CTF and 8 around the MAR; 2 earthquakes were found on the inactive part of the CFZ.

In this study, we present the first year-long catalogue of local seismicity around the equatorial MAR near the CTF, together with a 1D velocity model of the oceanic crust and upper mantle. The catalogue provides event times, hypocentre locations and magnitude information. We investigate small-scale seismicity variations along the CTF, the adjacent CFZ and the adjoining sections of the MAR. We also compute earthquake-magnitude distribution at CTF and RTF. Furthermore, we investigate the seismicity in relation to the depth of the brittle ductile region predicted by a simple thermal model (Harmon et al., 2018).

Method

Detection and location

120 The data were recorded by the 39 PI-LAB OBS stations during their one-year deployment
121 (Fig. 1, Table 1). The stations are mostly distributed in two lines north and south of the CTF
122 and eastern CFZ continuation with an average spacing of 40 km around the active part. On
123 the CTF, the typical minimum station distance to the events is around 50 km. Before working
124 with the continuous data, we checked the time stability at each station. Due to timing issues
125 L23D was excluded from the study. We use a Butterworth bandpass filter with corner
126 frequencies of 4Hz and 18Hz, which enhances the signal-to-noise ratio on OBS in a marine
127 environment. The a priori temporary set of picks is created using automated picks from a
128 short-time average divided by long time average (STA/LTA) detector. We use a 1D velocity
129 model that is based on CRUST1.0 (Laske et al., 2012), which includes an average regional
130 crustal thickness of around 8 km (Fig. 2A), plus a 2.90 km thick water layer, which
131 corresponds to the depth of the shallowest OBS location (S11D). Deeper than 35km, it is
132 based on ak135 (Kennett et al., 1995). Here, ST and LT time windows of 0.2s and 10s are
133 used, together with thresholds of 4 (trigger on) and 1.5 (trigger off). A minimum of 3 P- and
134 S-wave picks are set as a detection requirement. This results in 1492 a priori events with
135 11399 P- and 13948 S-picks.
136
137 The P- and S- picks are refined manually and iteratively in combination with an update on the
138 1-D velocity model and the event locations. Based on the picks the average v_P/v_S ratio is 1.73
139 (Fig. 2B). Dividing the picks by station and event origin region (Suppl. Fig. S1) reveals
140 deviations from that value. Events from the RTF have a v_P/v_S ratio of ~1.68 at all stations;
141 events from the western CTF have a v_P/v_S ratio of ~1.76 at stations located north of the
142 western CFZ. Event locations are computed using the NonLinLoc package (Lomax et al.,
143 2000). The package performs a probabilistic, non-linear global-search inversion using the list
144 of picked arrival times and a regional velocity model as input. Following the probabilistic

145 approach of Tarantola & Valette (1982) it calculates the hypocentre location using the
146 maximum likelihood of a probability density function of model parameters in the temporal
147 and spatial domain (event origin time and hypocentre location).
148
149 The velocity model is updated using VELEST3.1 (Kissling et al., 1994), which
150 simultaneously inverts for 1-D P- and S-wave velocities and hypocentral parameters. The
151 velocity model has a substantial influence on the depth accuracy, whereas lateral localisation
152 of most earthquakes can be constrained even if more general models are used. Further details
153 can be found in Appendix 1.
154
155 Given this we perform an additional test to verify the robustness of the depth estimates. We
156 compare NonLinLoc solutions with different maximum search depth limits (15, 20, 25, 30
157 km, as well 200 km, which we will label as "no limit"). When we used the "no limit" setting
158 of 200 km, in some instances NonLinLoc finds some very deep values. Therefore, we chose
159 different depth limits to evaluate the range of possibilities. Here, we present the greatest
160 depth that produces a reliable result, but also present the shallower solutions, to show the
161 uncertainties. We use the following steps to establish the preferred solution from the
162 NonLinLoc testing with different maximum search depth limits. Although the lateral
163 locations are typically the same regardless of the depth limit, we find a few solutions (~15%)
164 where the lateral location changes significantly with different depth limits. These outliers are
165 discarded for the remainder of the investigation; we then choose the location that has the
166 lowest root mean square (RMS) error if it is outside of error from the remaining location
167 solutions (see Suppl. Fig. S2 for an example). For locations where results using multiple
168 depth cut-offs are within error of each other and shallower than 30 km we use the solution
169 with the lowest RMS error. In cases where the lowest RMS error is reached at > 30 km depth

from the sea surface and the solution is within error of a shallower solution, we favour a shallower solution, but we mark the quality as marginal. We use 30 km depth as a cut-off because it corresponds to the approximate depth of the 900 – 1000˚ isotherms from simple thermal models (Harmon et al., 2018) based on the approximate length of the transform (900 km), the averaged half spreading rate (20 mm/yr) and the mantle potential (1350˚ C), which may be the limit of predicted brittle deformation (Molnar, 2020; Kohli et al., 2021). Although locations deeper than 30 km are generally unlikely, we will also present the deep solutions since deeper hypocentres have been found in other locations (McGuire et al., 2012; Kuna et al., 2019; Yu et al., 2021). To ensure the robustness of the computed depths are unbiased by heterogeneities due to long raypaths, we also carried out tests using only the data from the closest five stations with which an azimuthal gap below 180 degrees was still maintained. We did this on a random sampling of 6 events ranging from M_L of 3.3 to 5.6. The locations excluding longer paths were all within error of the original results.

Moment tensor inversion

For larger events, it is possible to carry out full moment tensor (MT) inversions, which provides additional constraints on the depth accuracy (e.g., Braunmiller & Nábělek, 2008). We use the Grond software tool (Heimann et al., 2018), which performs a Bayesian bootstrap-based inversion of the time-domain deviatoric MT. We only use the vertical component, which we found generally increases MT solution stability. The data are filtered between 12.5 s and 25 s. We fix our epicentral locations at those determined from the location inversion, for solution stability. In testing we find that if we relax this constraint the majority of epicentral locations are within the calculated uncertainties of one another. Differences arise in less than 5% of the solutions; these are more unstable due to noisy data,

thus resulting in a lack of stations with clear onset signals. Even in these cases the solutions are never more than 5 kilometres away from each other. We estimate the quality of these measurements based on the following parameters (Suppl. Figs. S3, S4): 1) the number of stations for which the theoretical waveforms fit the data is high, we assign quality level "MT best", respectively. 2) If the fits are generally poorer and/or the number of stations with good fits is lower than four, we categorise the event as "MT fair". 3) The stacked radiation patterns from different ensemble subsets of stations agree with each other (good agreement for best, overall agreement with potential outliers for fair). All solutions show a depth constraint that is well defined. In all cases where an MT solution exists, we use this depth estimate.

Magnitudes

We calculate local magnitudes for all the located earthquakes using amplitude measurements of the maxima on all components in a window of 150 s after the initial P-peak. After demeaning and detrending the data, we remove the instrument response and simulate the response of a Wood-Anderson seismometer (e.g., Bakun & Joyner, 1984; Hutton & Boore, 1987; Abercrombie, 1996). The data are then filtered using a high-pass filter with a corner frequency of 4 Hz to reduce oceanic noise. To account for further noise we introduce a signal-to-noise threshold of 1.3 for the zero-to-peak amplitude calculations that are used to compute local magnitudes. To account for changes in recorded amplitude with hypocentral distance due to geometric spreading and anelastic attenuation the event magnitudes are adjusted using the correction term:

$$\mathrm{Log}_{10}(A) - M_{ISC} = -1.46\,\mathrm{Log}_{10}(r/100) - 0.0016\,(r - 100) - 6.2 \qquad \text{(eq. 1)}$$

220 Here, A is the recorded amplitude, M_{ISC} is the magnitude as derived by the International
221 Seismological Centre (ISC), and r is the hypocentral distance. The term is derived in a similar
222 way as done in the work of Abercrombie et al. (1996), using an empirical comparison to our
223 MT solutions (Fig. 3).
224
225 *Earthquake magnitude-frequency distribution*
226
227 The earthquake magnitude-frequency distribution can be described by the b-value, which is
228 the gradient of the Gutenberg-Richter relationship ($\mathrm{Log}\{N(M)\} = a - bM$; Gutenberg &
229 Richter, 1944). The relationship shows that the number of events (N) above a certain
230 magnitude (M) can be expressed by two positive constants, representing the overall seismic
231 activity (a) and the relative occurrence of small to large magnitude earthquakes (b).
232
233 To calculate the b-value and associated uncertainties we use the maximum likelihood method
234 (Aki 1965; Utsu 1965; Bender 1983) in combination with a Kolmogorov-Smirnov test. The
235 catalogue is truncated at a magnitude of 2.3, which represents the magnitude of
236 completeness, M_C, along the CTF. The solution is accepted if the magnitude distribution and
237 the straight-line gradient b reach a similarity above M_C above a predetermined significance
238 level, in our case chosen to be rigorous at 20% (Schlaphorst et al., 2016).
239
240 **Results**
241
242 *Earthquake locations*
243

244 In total, 972 earthquakes could be located laterally (Fig. 4). Constraining depths with a larger
245 network spacing of around 40 km poses challenges, but we were able to constrain depths for
246 928 events. 118 could be constrained by applying an MT inversion (Fig. 4B; Suppl. Fig. S6).
247 Of the remaining event locations 650 are classified as good (Fig. 4C) and 150 are classified
248 as marginal quality (Fig. 4D). The majority of the MT constrained events (88) are located on
249 the CTF and CFZ. The lateral location uncertainty is smaller than the depth uncertainty with
250 a median value of $\tilde{y}$ = 2.86. Moment tensor solutions show the lowest depth uncertainties
251 with a median values of $\tilde{z}$ = 5.42 km in comparison with the median NonLinLoc solutions for
252 good ($\tilde{z}$ = 7.96 km) and marginal ($\tilde{z}$ = 11.87 km) categories (Fig. 4B, C, D). NonLinLoc
253 hypocentres are better constrained inside the network with the following median values of $\tilde{y}$
254 = 2.39 km and $\tilde{z}$ = 8.36 km for CTF in contrast to $\tilde{y}$ = 15.09 km and $\tilde{z}$ = 24.81 km for RTF.
255 Nearly all the events are found on or close to the OTFs (793) and the MAR (155). Only a
256 small number (10) are located on the inactive continuing CFZs. Another 13 can be found off
257 these features. Of the events located on or close to an OTF, 700 are close to the CTF, of
258 which the majority are concentrated towards the eastern side, particularly clustered towards
259 the ridge-transform intersection. A further 94 can be found around the RTF.
260
261 The earthquake depths determined using NonLinLoc, range from the seafloor to 43 km depth
262 beneath the sea surface. Most (716) are located shallower than 15 km depth. Events on the
263 MAR, away from the ridge-transform intersection, are mostly (36 out of 46) shallower than
264 10 km depth. Events on the MAR near the transform are deeper, with 12 events between 15
265 km and 30 km depth categorized as good. 60 events in the entire catalogue were located
266 between 30 and 40 km depth, of which only 4 are classified as good and 56 as marginal. 14
267 are located at depths greater than 40 km and all are categorised as marginal (Fig. 4D).
268

Focal mechanisms

Most of the MT depths are well-constrained (96 out of 118; Figs. 5, 6). Most solutions (63) are characterised by probability density functions (pdfs) with a clear singular peak. Some solutions (35) have a more complex distribution, but the dominant peak is shallow (<20 km). We find 20 events where a deep (20 – 49 km) MT solution exists that fits the waveforms equally well or better than a shallower solution (<20 km). We present both depths for completeness (Fig. 7). The deep solutions are likely unrealistic, given the expected maximum depth of brittle deformation (Molnar, 2020; Kohli et al., 2021), and so, we favour the shallower solution. In general, the deepest events are located along the CTF and RTF, while the events beneath the MAR are shallower than 12 km below sea level. There is only one event on the MAR that is deeper than 12 km. There is one intraplate earthquake with an MT solution located on the African plate near the CFZ, with a depth of 18 km.

MT inversion of 118 events in our catalogue shows a mix of strike slip, normal and reverse faults across the region (Fig. 5). Of the 88 focal mechanisms located on the CTF, the majority shows right lateral strike-slip movement (39), mostly dipping to the north. Towards the eastern end of the CTF, a combination of strike-slip and reverse faulting is observed (18). Several reverse faulting mechanisms can be observed in some locations along the CTF as well (20). Nearly all the 29 MAR events exhibit predominantly normal fault mechanisms with a minor strike-slip component in some cases. Furthermore, a rotation of the normal faulting axis can be observed close to ridge-transform intersections (Fig. 5; Suppl. Fig. S8). The one intraplate event on the CFZ has a moment tensor which shows normal faulting with fault plane solutions with north-south strike orientations

294 *Magnitudes*

295

296 We calculate local magnitudes from our catalogue (eq. 1) that range from 1.1 to 6.2. The
297 local 6.2 magnitude is a clipped estimate of the Romanche event, that was a larger Mw 7.1 in
298 the global CMT (Dziewonski et al., 1981; Ekström et al., 2012) and in a detailed local study
299 of the event (Hicks et al., 2020). The local magnitude scale clips for earthquakes of this large
300 magnitude, and the event is also outside of our array with a small backazimuthal coverage.
301 The next largest event in the catalogue is a M_L 5.6 located on the CTF. We note that our
302 relationship between amplitude and local magnitude scale (Fig. 3) resembles one derived for
303 the Azores (Gongóra et al., 2004), but also to the continental setting of southern California
304 (Hutton & Boore, 1987). Similarly, Kuna et al. (2019) found that the southern California
305 relationship fit the data recorded along the Blanco transform. It is likely that the tails of the
306 relationship curves are influenced by the number of distant events, since studies do not need
307 to consider the curve beyond their maximum event distance (e.g., Abercrombie, 1996;
308 Baumbach et al., 2003).

309

310 The moment magnitudes from MT inversion range from 3.0 to 6.2. This largest magnitude
311 corresponds to the M_w 7.1 Romanche event (Hicks et al., 2020). The magnitude is vastly
312 underestimated for four main reasons: 1) the large azimuthal gap, 2) the distance to the
313 network, 3) the usage of a CTF based velocity model and magnitude calibration, and 4) the
314 frequency range not being low enough for such large magnitude events. On the CTF three
315 M_w>5 events were located, the largest being a M_w 5.6. The largest earthquake that we
316 recorded on a MAR segment was a M_w 4.5, while the largest intraplate earthquake we
317 recorded was a M_w 3.2.

318

Earthquake magnitude-frequency distribution

The calculated *b*-value for the CTF is 0.81 ± 0.09 and for the RTF is 0.76 ± 0.22 (Fig. 8), so indistinguishable given the uncertainties. The network configuration results in large distances to the stations and azimuthal gaps for the events at the RTF, which leads to less well constrained magnitude estimations. These factors combined with the lower number of detected events leads to higher uncertainties for events at RTF. In addition, the magnitude of completeness is larger outside the network at the RTF (M_C = 3.4) compared to inside the network at CTF (M_C = 2.3). The RTF also has larger median local magnitudes (M_L = 3.7) compared to the CTF (M_L = 2.4). Within the CTF the median local M_L values vary, with M_L = 2.5 in the west and M_L = 2.3 in the east.

Discussion

Earthquake locations

The results generally show an expected pattern of event distribution. They are mostly located close to the ridge-transform plate tectonic boundary between the African and South American Plates. The sub-ridge events are located at depths shallower than 12 km beneath sea level. These likely occur in the crust and the uppermost mantle assuming around 3 km average water depth at the ridge and a 6-7 km average crustal thickness (Christeson et al., 2019), which is similar to a previous, shorter-term local study that found ~4.6 to 5.9 km thick crust to the west of the CTF using an OBS line perpendicular to the OTF direction (Marjanovic et al., 2020). These can be explained through extension of the crust due to seafloor spreading.

Earthquakes at slightly deeper depths than the crust beneath the ridge may occur given that geodynamic modelling suggests that lateral conductive cooling results in non-negligible thickness of the mantle lithosphere at slow spreading centres (Parmentier & Morgan, 1990). The deeper earthquakes observed along the transforms suggest that there is brittle deformation to greater depths than beneath the ridges. A deeper brittle-ductile transition beneath the transform in comparison to the ridges is predicted by the simple thermal model often used to describe a transform, created by averaging two opposing half-space cooling models. Here we show this model assuming a mantle potential temperature of 1350˚C and a thermal diffusivity of 10^{-6} mm^2/s (Harmon et al., 2018). Brittle deformation in the mantle lithosphere has also been observed in teleseismic estimates for CTF and RTF (Abercrombie & Ekström, 2001). The strain rate can be another component in controlling the depth extent of seismicity (Molnar, 2020).

Focal mechanisms

The focal mechanisms along the plate boundary are generally consistent with the ridge-transform system in the region. Specifically, we observe mostly normal fault MT solutions near the MAR segments, and mostly strike-slip solutions along the CTF and RTF consistent with the global view from the global CMT (Dziewonski et al., 1981; Ekström et al., 2012). The general pattern of north dipping focal mechanisms on the CTF and south dipping mechanisms on the RTF is in agreement with previous results that are based solely on teleseismic observations (Abercrombie & Ekström, 2001; Hicks et al., 2020; Yu et al., 2021). The reason for the opposite dip directions is unclear but could be related to the symmetry of the system and a transpressional stress regime that includes an anticlockwise rotation (Bonatti et al., 1994; Maia et al., 2016). At both ridge-transform intersections we observe the rotation

of the strike of the normal fault focal mechanism from ridge parallel on the ridge to around 35˚ off that orientation towards the strike direction of the OTF. This occurs over roughly 10 km at the eastern end and around 20 km on the western end (Suppl. Fig. S8). This rotation reflects the transition in stress regime as the plate boundary transitions from spreading to transform fault tectonics (Fox and Gallo, 1984) as predicted by geodynamic modelling (Morgan & Parmentier, 1984). This also results in the observed arcuate shaped scarps bending in towards the transform faults in the ridge-transform intersection in the CTF (Harmon et al. 2018).

The presence of reverse fault MT solutions in some parts of the CTF is indicative of transpression in the strike slip system. The reverse fault mechanisms are typically associated with topographic highs within the CTF, which have been interpreted as positive flower structures associated with restraining bends in the normal fault system (Harmon et al., 2018). The four positive flower structures have visible sharp scarps in the bathymetry (Harmon et al., 2018), and taken with the MT solutions, suggests that these are active features and the CTF is in active transpression today (Fig. 6). Transpression could be caused by a present-day rotation and re-adjustment of the African-South American spreading system. Previously, it has been suggested that the relative plate motions in the region have undergone a rotation of ~11° anticlockwise based on observations of transpressional features on the major OTFs to the north, for example Romanche and St. Paul, (Bonatti et al., 1994; Maia et al., 2016). Compressional mechanisms with fault planes roughly in SW-NE direction would be expected for the reorganisation/transpression direction, which can be observed for some but not all the moment tensor solutions. Still, our observations support these notions and suggest that the change in motions is ongoing.

Intraplate seismicity

The cluster of intraplate seismicity (5 events) observed on the CFZ on the African Plate at -11.5˚ longitude suggests there are internal stresses in the region of the earthquakes. The epicentres are very close (~5 km) to a M5.2 event recorded in the USGS catalogue on 14/04/2016 (before the OBS network deployment), hinting towards an ongoing process. The MT solution indicates a relatively deep event (18 km), suggesting strain is accumulating in the deeper part of the lithosphere, which caused brittle deformation there. The near vertical (or horizontal) fault plane and north-south strike direction are at odds with the expected tectonic fabric of the roughly east-west trending CFZ, so it does not appear to be re-activation of the fracture zone (FZ). Another example of a large intraplate oceanic earthquake in the Wharton Basin in the Indian Ocean was interpreted as FZ reactivation given that MT solutions were consistent with the FZ orientations (Yue et al., 2012), and the event may have been related to the nearby Sumatran subduction zone. One explanation for our event is that the intraplate stresses are due to the aforementioned rotation of the relative plate motions (Bonatti et al., 1994; Maia et al., 2016). It is also possible that strain caused by age differences leading to variations in plate thickness and/or density across the FZ cause that seismic activity (DeLong et al., 1977). However, we do not observe dip-slip faulting due to topography. Another potential explanation of intraplate stress in the region may be due to ocean mantle dynamics. Surface wave tomography and magnetotelluric imaging find a high velocity and high resistivity anomaly in this region centred at 12˚W and 0˚N (Fig. 4) with shear velocities of greater than 4.6 km/s at depths of 30 to 50 km (Saikia et al., 2021). This feature may be related to lithospheric heterogeneity and/or be the beginning of a lithospheric drip. We note that this feature is at shallower depths than the high velocity anomaly further east at 10.5˚W longitude (east of our research area) and 0˚N latitude with shear velocities of

419 greater than 4.4 km/s and $\log_{10}$ (resistivities) > 1.5 extending from 30 to 100 km depth that
420 was interpreted as a lithospheric drip (Harmon et al., 2020; 2021; Wang et al., 2020). The
421 lack of an observed receiver function phase from the lithosphere-asthenosphere boundary in
422 the latter location was interpreted as either the absence of melt ponding beneath the plate
423 and/or strong lithosphere-asthenosphere topography, again consistent with a drip (Rychert et
424 al., 2021). The observed vertical MT motion of the large event recorded in this region may be
425 consistent with the vertical stresses of the downwelling lithosphere (Fig. 5).
426
427 *Events beneath the 600˚C isotherm*
428
429 Some events beneath the CTF are located deeper than the predicted depth of the 600˚C
430 isotherm from half-space cooling, i.e., a greater depth than the previously proposed limit of
431 seismic slip at 600˚C based on teleseismic observations (Abercrombie & Ekström, 2001) and
432 earthquake rupture experiments (Boettcher et al., 2007). Earthquakes deeper than expected
433 based on isotherms predicted for an oceanic transform from the half-space cooling model
434 have also been observed at Blanco (Kuna et al., 2019), Gofar (McGuire et al., 2012) and
435 Romanche (Yu et al., 2021). These observations are typically interpreted as lithospheric
436 cooling caused by hydrothermal circulation, which can deepen the depth of the brittle-ductile
437 transition (Roland et al., 2010). In some cases, the events were deeper than expected by
438 numerical modelling accounting for hydrothermal circulation (Roland et al., 2010; McGuire
439 et al., 2012; Kuna et al., 2019). Alternatively, lateral variability in composition might have an
440 influence on the seismicity. A likely explanation for the CTF is that brittle and ductile
441 deformation can occur over a broad range of temperatures (300˚C – 900˚/1000˚C) and,
442 therefore, a broad range of depths, owing to variable seawater infiltration and grain sizes

along the fault. This is supported by observations of exhumed hydraulically altered mylonites (Molnar, 2020; Kohli et al., 2021).

Earthquake magnitude-frequency distribution

The *b*-value of the entire catalogue of CTF events is lower than the global average value of 1.0 but in agreement with the results from a previous study of tidal triggering in the Mid-Atlantic segment just north of the CTF (Leptokaropoulos et al., 2021). The low *b*-value (0.81 ± 0.09) also supports the notion that average coupling along the CTF is low and that much of the strain is accommodated aseismically. However, historical seismicity, which has resulted in several large events (Mw > 6.5), suggests that coupling in discrete locations may be higher (Shi et al., 2021). This agrees with results from Blanco Transform, where crustal *b*-values are similarly low ($b = 0.78 \pm 10$) and coupling is low but variable along the fault (Kuna et al., 2019). A study of different plate boundary settings found similarities between magnitude-frequency relationships of OTFs and continental TFs (Bird & Kagan, 2003).

Cumulative moment release

We compare the cumulative moment release over the 1-year of our array to examine the average seismic coupling. We find that the cumulative moment release on the CTF was 4.9 x 10^{17} Nm. The release on the RTF was 5.7 x 10^{19} Nm. The release on the ridge segments had a cumulative moment of 3.3 x 10^{16} Nm. The higher release on the Romanche is due to the M_w 7.1 event and its aftershock sequence. A more detailed investigation of this event is presented in (Hicks et al., 2020). The predicted moment release per year for the thermal lithosphere from Boettcher and Jordan, (2004) for the CTF is 5.6 x 10^{19} Nm yr^{-1}, which suggests only

~1% of the predicted moment release was released seismically over the year-long observation period. Our results also support the notion that the CTF is relatively weak and not coupled. In contrast, continental TFs show higher amounts of seismic coupling (Bird & Kagan, 2003). Low coupling values of normally around 10–30% have been observed for OTFs around the world, although showing large variability (Boettcher & Jordan, 2016), and a consensus of a general inverse correlation between seismic coupling and spreading rate has been found (e.g., Kawasaki et al., 1985; Sobolev & Rundquist, 1999). For many OTFs in the Atlantic, higher values have been observed (e.g., Gibbs, Oceanographer, 15-20 OTF – Muller, 1983; Kane OTF — Wilcock et al., 1990), which all have a present-day full spreading rate between 21 and 26 mm/yr (DeMets et al., 1994), slightly slower than the CTF. However, low values have been found as well (e.g., Vema, Kane, Doldrums OTF – Muller, 1983), which, apart from the Kane OTF, have spreading rates between 28 and 33 mm/yr. Uncertainties can arise due to shortness of the observation duration, as well as a large estimation of annual moment release due to the choice of OTF dimensions (Muller, 1983; Wilcock et al., 1990). For the entire Romanche, the predicted value of cumulative moment release from the thermal lithosphere is 2.9×10^{19} Nm yr^{-1}, approximately half of the observed moment release. Large events like the M_w 7.1 occur relatively rarely, approximately every 30 years on Romanche, indicating the moment release during this time was particularly high. Given that these large events occur on different segments, and do not rupture the entire length of the transform fault, portions of the RTF likely have high seismic coupling. This observation also highlights the temporal variability of moment release on OTFs. The MAR segments show a very low cumulative moment (3.3×10^{16} Nm) compared to the OTFs (>=4.9×10^{17} Nm) in the region for the duration of the deployment, which may suggest that the normal faulting also has a low coupling during this time period.

Conclusions

We present an earthquake catalogue from a broadband ocean bottom seismic experiment from March 2016 to March 2017 at the equatorial MAR centred around the CFZ, which provides one of the first detailed seismicity studies from a larger local network around a slow moving OTF. Most of the events are located on the South American – African Plate boundary as expected although we also recorded 10 events near the CFZ, east of the OTF and 13 additional intraplate earthquakes. Focal mechanisms on the MAR are predominantly characterised as normal faulting and on the OTF they are predominantly strike slip as expected. A few (17) predominantly reverse faulting mechanisms on the transform are likely caused by a transpressional stress regime related to current rotation of the ridge-transform system. The focal mechanism of an intraplate event on the CFZ shows vertical displacement, consistent with a hypothesized nearby lithospheric drip. The magnitudes range from 1.1 to 5.6 and we find a *b*-value of 0.81 ± 0.09 for the CTF. The earthquakes on the ridge are limited to the crust and the shallowest mantle (< 12 km depth) while the events on the CTF are deeper, with high quality MT location depths of up to 26 km beneath the sea surface, which is much deeper than the depth of the brittle-ductile transition predicted for simple thermal models. A simple thermal model cannot explain these deeper events, and another factor is required, for instance, lithospheric cooling by hydrothermal circulation.

Acknowledgements

All images were produced using GMT (Wessel et al., 2013). Additional information about SDX can be found at www.liv.ac.uk/~aeh/index.html. D.S. would like to acknowledge the financial support FCT through project UIDB/50019/2020 – IDL. C.A.R. and N.H. acknowledge funding from from the Natural Environment Research Council (NE/M003507/1), the European Research Council (GA 638665). C.A.R. acknowledges funding from from the National Science Foundation (NSF-EAR-2147918). J.-M. Kendall was funded by the Natural Environment Research Council (NE/M004643/1).

D.S. managed the study and carried out the locating. C.A.R. and N.H. conceived the experiment, acquired funding, managed the project, and contributed to the manuscript. S.P.H. created the initial automated detection of events, assisted with the locations, and commented on the manuscript. P.B. worked on event depth improvements and commented on the manuscript. J.M.K. co-managed the project and commented on the manuscript. R.E.A. contributed to improving the event localization method and commented on the manuscript.

Data Availability

The continuous raw seismic waveform data from the PI-LAB OBS network is available to download from IRIS Data Management Center (https://doi.org/10.7914/SN/XS_2016).

Appendix 1 – Details on iterative pick refinement, model update and event localisation in NonLinLoc

In step 1, P- and S-arrivals are readjusted using the vertical component and the Seismic Analysis Code (SAC). This is done without the implementation of calculated theoretical arrival times derived from the automated picks in order to keep the reassessed picks unbiased. Although different filters as well as the unfiltered data are used to evaluate potential onsets,

538 we use the same corner frequencies to determine the onsets to have consistent P- and S-
539 moveouts and P-to-S travel time differences. The weighting of picks is assigned to reflect
540 their quality, using levels from 0 (highest) to 4 (lowest). The levels are associated with an
541 uncertainty in arrival time, using values of 0.1s, 0.2s, 0.5s, 0.8s, and 1.5s (Hicks et al., 2014).
542 Picks of quality level 4 are subsequently omitted from the locating process.
543
544 In step 2, the event locations are computed using the NonLinLoc package (Lomax et al.,
545 2000). The package performs a probabilistic, non-linear global-search inversion using the list
546 of picked arrival times and a regional velocity model as input. Following the probabilistic
547 approach of Tarantola & Valette (1982) it calculates the hypocentre location using maximum
548 likelihood of a probability density function of model parameters in the temporal and spatial
549 domain. The initial velocity model is given by CRUST1.0 resulting in an average regional
550 crustal thickness of around 8 km (Fig. 2A), plus a 2.90 km thick water layer, which
551 corresponds to the depth of the shallowest OBS location (S11D). We do not include a
552 sediment layer since it is supposed to be very thin in the area (Agius et al., 2018; Saikia et al.,
553 2020). In this step, we also combine picks that are counted as multiple events by the
554 STA/LTA detector, thus reducing the overall number of events.
555
556 A minimum of 3 stations with clearly observable and coherent arrivals is required to identify
557 the event. We use a search grid spacing of 1km in all three dimensions and an average v_P/v_S
558 ratio of 1.73, based on picked P–S arrival time differences (Fig. 2B). The quality of the
559 resulting location is based on temporal uncertainty (i.e., root mean square or RMS error) as
560 well as spatial uncertainty. The latter is a combination of the size of the ellipsoidal
561 approximation to the 1σ confidence level of the location likelihood scatter and the overall
562 shape of the scatter sample. Lateral localisation of most earthquakes can be constrained

563 relatively precisely, even if more general models are used, whereas the velocity model has a
564 larger impact on depth localisation.
565
566 In step 3, the picks of events with low quality are refined. This includes all events that either
567 have large location uncertainty and/or where picks and theoretical arrival times show large
568 mismatches. Here we use the Seismic Data eXplorer (SDX; Hicks et al., 2014), additionally
569 including the two horizontal components and the hydrophone component. SDX updates
570 theoretical onset time calculations of P- and S-phases automatically after each change of pick
571 placement. In general, this reduces the number of mispicks. There are, however, instances,
572 where clearly identifiable onsets do not match the theoretical arrivals. In most cases, this is
573 due to an inaccurate velocity model.
574
575 In step 4, the velocity model is updated, based on the updated set of picks. We use the
576 program VELEST3.1 (Kissling et al., 1994), which simultaneously inverts for 1D P- and S-
577 wave velocities and hypocentral parameters. For this step, we concentrate on the picks of
578 events on or close to the CTF. This ensures good azimuthal coverage with a gap of less than
579 180˚. Also, regional heterogeneities are likely to distort a uniform velocity model if the area
580 is chosen too large and diverse. We limit the selection further to events with an RMS of less
581 than 1.2, a minimum number of P-picks of 5, and a minimum number of S picks of 3.
582
583 Steps 2, 3 and 4 are run iteratively until the model and arrival time picks stabilise. Here, three
584 iterations proved to be sufficient.
585

586 **References**

587 Abercrombie, R. E. (1996). The magnitude-frequency distribution of earthquakes recorded
588 with deep seismometers at Cajon Pass, southern California. Tectonophysics, 261(1-3), 1-7.
589 DOI: 10.1016/0040-1951(96)00052-2.
590
591 Abercrombie, R. E., & Ekström, G. (2001). Earthquake slip on oceanic transform faults.
592 Nature, 410(6824), 74-77. DOI: 10.1038/35065064.
593
594 Agius, M. R., N. Harmon, C. A. Rychert, S. Tharimena, and J. M. M. Kendall (2018),
595 Sediment characterization at the equatorial Mid-Atlantic Ridge from P-to-S teleseismic phase
596 conversions recorded on the PI-LAB experiment, Geophys. Res. Lett., 45, 12,244–12,252.
597 DOI: 10.1029/2018GL080565.
598
599 Agius, M. R., Rychert, C. A., Harmon, N., Tharimena, S., & Kendall, J. (2021). A thin
600 mantle transition zone beneath the equatorial Mid-Atlantic Ridge. Nature, 589(7843), 562-
601 566. DOI: 10.1038/s41586-020-03139-x.
602
603 Aki, K. (1965). Maximum likelihood estimate of b in the formula logN= a-bM and its
604 confidence limits. Bull. Earthquake Res. Inst. Univ. Tokyo, 43, 237-239.
605
606 Amante, C., & Eakins, B. W. (2009). ETOPO1 arc-minute global relief model: procedures,
607 data sources and analysis. DOI: 10.7289/V5C8276M.
608
609 Bakun, W. H., & Joyner, W. B. (1984). The M_L scale in central California. Bulletin of the
610 Seismological Society of America, 74(5), 1827-1843. DOI: 10.1785/BSSA0740051827.

Baumbach, M., Bindi, D., Grosser, H., Milkereit, C., Parolai, S., Wang, R., ... & Zschau, J. (2003). Calibration of an ML scale in northwestern Turkey from 1999 Izmit aftershocks. Bulletin of the Seismological Society of America, 93(5), 2289-2295. DOI: 10.1785/0120020157.

Behn, M. D., Boettcher, M. S., & Hirth, G. (2007). Thermal structure of oceanic transform faults. Geology, 35(4), 307-310. DOI: 10.1130/G23112A.1.

Bender, B. (1983). Maximum likelihood estimation of b values for magnitude grouped data. Bulletin of the Seismological Society of America, 73(3), 831-851. DOI: 10.1785/BSSA0730030831.

Bergman, E. A., & Solomon, S. C. (1988). Transform fault earthquakes in the North Atlantic: Source mechanisms and depth of faulting. Journal of Geophysical Research: Solid Earth, 93(B8), 9027-9057. DOI: 10.1029/JB093iB08p09027.

Bird, P. (2003). An updated digital model of plate boundaries. Geochemistry, Geophysics, Geosystems, 4(3). DOI: 10.1029/2001GC000252.

Bird, P., & Kagan, Y. Y. (2004). Plate-tectonic analysis of shallow seismicity: Apparent boundary width, beta, corner magnitude, coupled lithosphere thickness, and coupling in seven tectonic settings. Bulletin of the Seismological Society of America, 94(6), 2380-2399. DOI: 10.1785/0120030107.

636 Boettcher, M. S., Hirth, G., & Evans, B. (2007). Olivine friction at the base of oceanic
637 seismogenic zones. Journal of Geophysical Research: Solid Earth, 112(B1). DOI:
638 10.1029/2006JB004301.
639
640 Boettcher, M. S., & Jordan, T. H. (2004). Earthquake scaling relations for mid-ocean ridge
641 transform faults. Journal of Geophysical Research: Solid Earth, 109(B12). DOI:
642 10.1029/2004JB003110.
643
644 Bogiatzis, P., Karamitrou, A., Ward Neale, J., Harmon, N., Rychert, C. A., & Srokosz, M.
645 (2020). Source regions of infragravity waves recorded at the bottom of the equatorial Atlantic
646 Ocean, using OBS of the PI-LAB experiment. Journal of Geophysical Research: Oceans,
647 125(6), e2019JC015430. DOI: 10.1029/2019JC015430.
648
649 Bonatti, E., Ligi, M., Gasperini, L., Peyve, A., Raznitsin, Y. U., & Chen, Y. J. (1994).
650 Transform migration and vertical tectonics at the Romanche fracture zone, equatorial
651 Atlantic. Journal of Geophysical Research: Solid Earth, 99(B11), 21779-21802. DOI:
652 10.1029/94JB01178.
653
654 Braunmiller, J., & Nábělek, J. (2008). Segmentation of the Blanco Transform Fault Zone
655 from earthquake analysis: Complex tectonics of an oceanic transform fault. Journal of
656 Geophysical Research: Solid Earth, 113(B7). DOI: 10.1029/2007JB005213.
657
658 Christeson, G. L., J. A. Goff, and R. S. Reece (2019), Synthesis of Oceanic Crustal Structure
659 From Two-Dimensional Seismic Profiles, Reviews of Geophysics, 57(2), 504-529.
660 DOI:10.1029/2019RG000641.

661

662 Delong, S. E., & Fox, P. J. (1977). Geological consequences of ridge subduction. Island arcs,
663 deep sea trenches and back-arc basins, 1, 221-228. DOI: 10.1029/ME001p0221.
664

665 DeMets, C., Gordon, R. G., Argus, D. F., & Stein, S. (1994). Effect of recent revisions to the
666 geomagnetic reversal time scale on estimates of current plate motions. Geophysical research
667 letters, 21(20), 2191-2194. DOI: 10.1029/94GL02118.
668

669 Dziewonski, A. M., T.-A. Chou and J. H. Woodhouse, Determination of earthquake source
670 parameters from waveform data for studies of global and regional seismicity, J. Geophys.
671 Res., 86, 2825-2852, 1981. DOI:10.1029/JB086iB04p02825.
672

673 Ekström, G., M. Nettles, and A. M. Dziewonski, The global CMT project 2004-2010:
674 Centroid-moment tensors for 13,017 earthquakes, Phys. Earth Planet. Inter., 200-201, 1-9,
675 2012. DOI:10.1016/j.pepi.2012.04.002.
676

677 Engeln, J. F., Wiens, D. A., & Stein, S. (1986). Mechanisms and depths of Atlantic transform
678 earthquakes. Journal of Geophysical Research: Solid Earth, 91(B1), 548-577. DOI:
679 10.1029/JB091iB01p00548.
680

681 Fischer, K. M., H. L. Ford, D. L. Abt, and C. A. Rychert (2010) The lithosphere-
682 asthenosphere boundary, Ann. Rev. Earth and Planet. Sci., 38: 551-575,
683 DOI:10.1146/annurev-earth-040809-152438.
684

685 Fischer, K. M., C. A. Rychert, C. Dalton, M. Miller, C. Beghein, D. Schutt (2020) A
686 comparison of oceanic and continental mantle lithosphere, Phys. Earth & Planet. Int., CIDER
687 special ed., DOI:10.1016/j.pepi.2020.106600.
688
689 Fox, P. J., & Gallo, D. G. (1984). A tectonic model for ridge-transform-ridge plate
690 boundaries: Implications for the structure of oceanic lithosphere. Tectonophysics, 104(3-4),
691 205-242. DOI: 10.1016/0040-1951(84)90124-0.
692
693 Góngora, E., Carrilho, F., & Oliveira, C. S. (2004). Calibration of local magnitude ML in the
694 Azores archipelago based on recent digital recordings. Pure and Applied Geophysics, 161(3),
695 647-659. DOI: 10.1007/s00024-003-2467-0.
696
697 Gregory, E. P., Singh, S. C., Marjanović, M., & Wang, Z. (2021). Serpentinized peridotite
698 versus thick mafic crust at the Romanche oceanic transform fault. Geology, 49(9), 1132-
699 1136. DOI: 10.1130/G49097.1.
700
701 Grevemeyer, I., Reston, T. J., & Moeller, S. (2013). Microseismicity of the Mid-Atlantic
702 Ridge at 7° S–8° 15′ S and at the Logatchev Massif oceanic core complex at 14° 40′ N–14°
703 50′ N. Geochemistry, Geophysics, Geosystems, 14(9), 3532-3554. DOI: 10.1002/ggge.20197.
704
705 Gutenberg, B. and Richter, C.E, 1944. Frequency of earthquakes in California. Bull. Seismol.
706 Soc. Am., 34: 185-188. DOI: 10.1785/BSSA0340040185.
707
708 Harmon, N., Rychert, C., Agius, M., Tharimena, S., Le Bas, T., Kendall, J. M., & Constable,
709 S. (2018). Marine geophysical investigation of the chain fracture zone in the Equatorial

710 Atlantic from the PI-LAB experiment. Journal of Geophysical Research: Solid Earth,
711 123(12), 11-016. DOI: 10.1029/2018JB015982.
712
713 Harmon, N., C. A. Rychert, J. M. Kendall, M. Agius, P. Bogiatzis, and S. Tharimena (2020),
714 Evolution of the oceanic lithosphere in the equatorial Atlantic from Rayleigh wave
715 tomography, evidence for small-scale convection from the PI-LAB experiment, Geochem.
716 Geophys. Geosys., 21, e2020GC009174.
717
718 Harmon, N., Wang, S., Rychert, C. A., Constable, S., & Kendall, J. M. (2021). Shear velocity
719 inversion guided by resistivity structure from the PI-LAB Experiment for integrated estimates
720 of partial melt in the mantle. Journal of Geophysical Research: Solid Earth, 126(8),
721 e2021JB022202. DOI: 10.1029/2021JB022202.
722
723 Harmon, N., G. Laske, W. Crawford, and C. A. Rychert (2022) Tilt corrections for normal
724 mode observations on ocean bottom seismic data, an example from the PI-LAB experiment,
725 Seismica, DOI:10.26443/seismica.v1i1.196.
726
727 Heimann, S., Isken, M., Kühn, D., Sudhaus, H., Steinberg, A., Daout, S., Cesca, S., Bathke,
728 H., Dahm, T. (2018). Grond: a probabilistic earthquake source inversion framework,
729 Potsdam: GFZ Data Services. DOI:10.5880/GFZ.2.1.2018.003.
730
731 Hicks, S. P., Rietbrock, A., Ryder, I. M., Lee, C. S., & Miller, M. (2014). Anatomy of a
732 megathrust: The 2010 M8. 8 Maule, Chile earthquake rupture zone imaged using seismic
733 tomography. Earth and Planetary Science Letters, 405, 142-155. DOI:
734 10.1016/j.epsl.2014.08.028.

735

736 Hicks, S. P., Okuwaki, R., Steinberg, A., Rychert, C. A., Harmon, N., Abercrombie, R. E., …
737 & Sudhaus, H. (2020). Back-propagating supershear rupture in the 2016 M_W 7.1 Romanche
738 transform fault earthquake. Nature Geoscience, 13(9), 647-653. DOI: 10.1038/s41561-020-
739 0619-9.

740

741 Hutton, L. K., & Boore, D. M. (1987). The M_L scale in southern California. Bulletin of the
742 Seismological Society of America, 77(6), 2074-2094. DOI: 10.1785/BSSA0770062074.

743

744 Illsley-Kemp, F., Keir, D., Bull, J. M., Ayele, A., Hammond, J. O., Kendall, J. M., ... &
745 Goitom, B. (2017). Local earthquake magnitude scale and b-value for the Danakil region of
746 northern Afar. Bulletin of the Seismological Society of America, 107(2), 521-531. DOI:
747 10.1785/0120150253.

748

749 Kawasaki, I., Kawahara, Y., Takata, I., & Kosugi, N. (1985). Mode of seismic moment
750 release at transform faults. Tectonophysics, 118(3-4), 313-327. DOI: 10.1016/0040-
751 1951(85)90131-3.

752

753 Kennett, B.L.N. Engdahl, E.R. & Buland R., 1995. Constraints on seismic velocities in the
754 Earth from travel times, Geophys J Int, 122, 108-124. DOI: 10.1111/j.1365-
755 246X.1995.tb03540.x.

756

757 Kissling, E., W.L. Ellsworth, D. Eberhart-Phillips, and U. Kradolfer (1994). Initial reference
758 models in local earthquake tomography, J. Geophys. Res., 99, 19635-19646. DOI:
759 10.1029/93JB03138.

760

761 Kohli, A., Wolfson-Schwehr, M., Prigent, C., & Warren, J. M. (2021). Oceanic transform
762 fault seismicity and slip mode influenced by seawater infiltration. Nature Geoscience, 14(8),
763 606-611. DOI: 10.1038/s41561-021-00778-1.

764

765 Kuna, V. M., Nábělek, J. L., & Braunmiller, J. (2019). Mode of slip and crust–mantle
766 interaction at oceanic transform faults. Nature Geoscience, 12(2), 138-142. DOI:
767 10.1038/s41561-018-0287-1.

768

769 Langston, C. A., Brazier, R., Nyblade, A. A., & Owens, T. J. (1998). Local magnitude scale
770 and seismicity rate for Tanzania, East Africa. Bulletin of the Seismological Society of
771 America, 88(3), 712-721. DOI: 10.1785/BSSA0880030712.

772

773 Laske, G., Masters., G., Ma, Z. and Pasyanos, M., Update on CRUST1.0 – A 1-degree Global
774 Model of Earth's Crust, Geophys. Res. Abstracts, 15, Abstract EGU2013-2658, 2013.

775

776 Leptokaropoulos, K., Harmon, N., Hicks, S. P., Rychert, C. A., Schlaphorst, D., & Kendall, J.
777 M. (2021). Tidal Triggering of Microseismicity at the Equatorial Mid-Atlantic Ridge,
778 Inferred From the PI-LAB Experiment. Journal of Geophysical Research: Solid Earth,
779 126(9), e2021JB022251. DOI: 10.1029/2021JB022251.

780

781 Leptokaropoulos, K., C. A. Rychert, N. Harmon, J. M. Kendall (2023) Seismicity properties
782 of the Chain Transform Fault inferred using data from the PI-LAB experiment J Geophys
783 Res, DOI:10.1029/2022JB024804.

784

Lomax, A., J. Virieux, P. Volant and C. Berge, (2000), Probabilistic earthquake location in 3D and layered models: Introduction of a Metropolis-Gibbs method and comparison with linear locations, in Advances in Seismic Event Location, Thurber, C.H., and N. Rabinowitz (eds.), Kluwer, Amsterdam, 101-134. DOI: 10.1007/978-94-015-9536-0_5.

Maia, M., Sichel, S., Briais, A., Brunelli, D., Ligi, M., Ferreira, N., ... & Oliveira, P. (2016). Extreme mantle uplift and exhumation along a transpressive transform fault. Nature Geoscience, 9(8), 619-623. DOI: 10.1038/ngeo2759.

Marjanović, M., Singh, S. C., Gregory, E. P., Grevemeyer, I., Growe, K., Wang, Z., ... & Filbrandt, C. (2020). Seismic crustal structure and morphotectonic features associated with the Chain Fracture Zone and their role in the evolution of the equatorial Atlantic region. Journal of Geophysical Research: Solid Earth, 125(10), e2020JB020275. DOI:10.1029/2020JB020275.

McGuire, J. J., Collins, J. A., Gouédard, P., Roland, E., Lizarralde, D., Boettcher, M. S., ... & Van Der Hilst, R. D. (2012). Variations in earthquake rupture properties along the Gofar transform fault, East Pacific Rise. Nature Geoscience, 5(5), 336-341. DOI: 10.1038/ngeo1454.

Molnar, P. (2020). The brittle-plastic transition, earthquakes, temperatures, and strain rates. Journal of Geophysical Research: Solid Earth, 125(7), e2019JB019335. DOI: 10.1029/2019JB019335.

809 Morgan, J. P., & Parmentier, E. M. (1984). Lithospheric stress near a ridge-transform
810 intersection. Geophysical Research Letters, 11(2), 113-116. DOI:
811 10.1029/GL011i002p00113.
812
813 Muller, J. L. (1983). Earthquake source parameters, seismicity, and tectonics of North
814 Atlantic transform faults (Doctoral dissertation, Massachusetts Institute of Technology).
815
816 Müller, R. D., Sdrolias, M., Gaina, C., & Roest, W. R. (2008). Age, spreading rates, and
817 spreading asymmetry of the world's ocean crust. Geochemistry, Geophysics, Geosystems,
818 9(4). DOI: 10.1029/2007GC001743.
819
820 Ottemöller, L., & Sargeant, S. (2013). A local magnitude scale ML for the United Kingdom.
821 Bulletin of the Seismological Society of America, 103(5), 2884-2893. DOI:
822 10.1785/0120130085.
823
824 Parmentier, E. M., & Morgan, J. P. (1990). Spreading rate dependence of three-dimensional
825 structure in oceanic spreading centres. Nature, 348(6299), 325-328. DOI: 10.1038/348325a0.
826
827 Parnell-Turner, R., Smith, D. K., & Dziak, R. P. (2022). Hydroacoustic monitoring of
828 seafloor spreading and transform faulting in the equatorial Atlantic Ocean. Journal of
829 Geophysical Research: Solid Earth, 127(7), e2022JB024008. DOI: 10.1029/2022JB024008.
830
831 Richter, C. F. (1935). An instrumental earthquake magnitude scale, Bull. Seism. Soc. Am. 25,
832 1-31. DOI: 10.1785/BSSA0250010001.
833

834 Richter, C. F. (1958). Elementary Seismology, W. H. Freeman and Co., San Francisco,
835 California, 578 pp.
836
837 Roland, E., Behn, M. D., & Hirth, G. (2010). Thermal-mechanical behavior of oceanic
838 transform faults: Implications for the spatial distribution of seismicity. Geochemistry,
839 Geophysics, Geosystems, 11(7). DOI: 10.1029/2010GC003034.
840
841 Rychert, C. A., K. M. Fischer, and S. Rondenay (2005), A sharp lithosphere-asthenosphere
842 boundary imaged beneath eastern North America, Nature, 436, 542-545,
843 doi:10.1038/nature03904.
844
845 Rychert, C. A., S. Rondenay, and K. M. Fischer (2007), P-to-S and S-to-P imaging of a sharp
846 lithosphere-asthenosphere boundary beneath eastern North America, J. Geophys. Res., 112,
847 B08314, doi:10.1029/2006JB004619.
848
849 Rychert, C. A., P. M. Shearer, and K. M. Fischer (2010) Scattered wave imaging of the
850 lithosphere-asthenosphere boundary, Lithos, doi:10.1016/j.lithos.2009.12.006.
851
852 Rychert, C. A., Kendall, J. M., & Harmon, N. (2016). Passive Imaging of the Lithosphere-
853 Asthenosphere Boundary. DOI:10.7914/SN/XS_2016.
854
855 Rychert, C. A., N. Harmon, and *S. Tharimena (2018a), Seismic Imaging of the base of the
856 ocean plates, in Lithospheric Discontinuities, edited by H. Yuan & B. Romanowicz, AGU
857 Monographs, Washington DC, DOI:10.1002/9781119249740.ch4.
858

Rychert, C. A., N. Harmon, and *S. Tharimena (2018b) Scattered wave imaging of the oceanic plate in Cascadia, Science Advances, doi:10.1126/sciadv.aao1908.

Rychert, C. A., N. Harmon, S. Constable, S. Wang (2020) The nature of the lithosphere-asthenosphere boundary, J. Geophys. Res. Grand Challenges Centennial Collection, doi:10.1029/2018JB016463.

Rychert, C. A., Tharimena, S., Harmon, N., Wang, S., Constable, S., Kendall, J. M., ... & Schlaphorst, D. (2021). A dynamic lithosphere–asthenosphere boundary near the equatorial Mid-Atlantic Ridge. Earth and Planetary Science Letters, 566, 116949. DOI: 10.1016/j.epsl.2021.116949.

Rychert, C. A. and P. M. Shearer (2009) A global view of the lithosphere- asthenosphere boundary, Science, 324, DOI:10.1126/science.1169754.

Saikia, U., C. Rychert, N. Harmon and J.M. Kendall (2020), Sediment structure at the equatorial mid atlantic ridge constrained by seafloor admittance using data from the PI LAB experiment, Mar. Geophys. Res., 41, 3, doi: 10.1007/s11001-020-09402-0.

Saikia, U., C. Rychert, N. Harmon, and J. M. Kendall (2021), Upper mantle anisotropic shear velocity structure at the equatorial Mid-Atlantic ridge constrained by Rayleigh wave group velocity analysis from the PI-LAB experiment, Geochem. Geophys. Geosys., 22, e2020GC009495, DOI: 10.1029/2020GC009495.

Saunders, I., Ottemöller, L., Brandt, M. B., & Fourie, C. J. (2013). Calibration of an ML scale for South Africa using tectonic earthquake data recorded by the South African National Seismograph Network: 2006 to 2009. Journal of seismology, 17(2), 437-451. DOI: 10.1007/s10950-012-9329-0.

Schlaphorst, D., Kendall, J. M., Collier, J. S., Verdon, J. P., Blundy, J., Baptie, B., ... & Bouin, M. P. (2016). Water, oceanic fracture zones and the lubrication of subducting plate boundaries—insights from seismicity. Geophysical Journal International, 204(3), 1405-1420. DOI: 10.1093/gji/ggv509.

Shi, P., Meng W. & Pockalny, R. The ubiquitous creeping segments on oceanic transform faults, Geology 50, 199-204 (2021). DOI: 10.1130/G49562.1.

Slemmons, D. B., & Depolo, C. M. (1986). Evaluation of active faulting and associated hazards. Active Tectonics, 1986, 45-62.

Sobolev, P. O., & Rundquist, D. V. (1999). Seismicity of oceanic and continental rifts—A geodynamic approach. Physics of the earth and planetary interiors, 111(3-4), 253-266. DOI: 10.1016/S0031-9201(98)00165-4.

Tarantola, A. and Valette, B., 1982, Inverse problems = quest for information., J. Geophys., 50, 159-170.

906 Tharimena, S., C. A. Rychert and N. Harmon (2016) Seismic Imaging of a mid-lithospheric
907 discontinuity beneath Ontong Java Plateau, Earth & Planet. Sci. Lett., 450, 62-70,
908 doi:10.1016/j.epsl.2016.06.026
909
910 Tharimena, S., C. A. Rychert, and N. Harmon (2017a) A unified continental thickness from
911 seismology and diamonds suggests a melt-defined plate, Science, 357, 6351, pp. 580-583,
912 doi:10.1126/science.aan0741.
913
914 Tharimena, S., C. A. Rychert, and N. Harmon (2017b) Imaging the Pacific lithosphere –
915 Insights from SS Precursor modeling, J. Geophys. Res., doi:10.1002/2016JB013526.
916
917 Toomey, D. R., Solomon, S. C., & Purdy, G. M. (1988). Microearthquakes beneath median
918 valley of Mid-Atlantic Ridge near 23° N: Tomography and tectonics. Journal of Geophysical
919 Research: Solid Earth, 93(B8), 9093-9112. DOI: 10.1029/JB093iB08p09093.
920
921 Utsu, T. (1965). A method for determining the value of" b" in a formula log n= a-bM
922 showing the magnitude-frequency relation for earthquakes. Geophys. Bull. Hokkaido Univ.,
923 13, 99-103.
924
925 Wang, S., S. Constable, V. Reyes-Ortega, C. A. Rychert (2019) A marine magnetotelluric
926 coast effect sensitive to the lithosphere-asthenosphere boundary, Geophys. J. Int.,
927 DOI:10.1093/gji/ggz202.
928
929 Wang, S., Constable, S., Rychert, C. A., & Harmon, N. (2020). A lithosphere-asthenosphere
930 boundary and partial melt estimated using marine magnetotelluric data at the central Middle

931 Atlantic Ridge. Geochemistry, Geophysics, Geosystems, 21(9), e2020GC009177. DOI:
932 10.1029/2020GC009177.
933
934 Wessel, P., W. H. F. Smith, R. Scharroo, J. Luis, and F. Wobbe, Generic Mapping Tools:
935 Improved Version Released, EOS Trans. AGU, 94(45), p. 409–410, 2013.
936 DOI:10.1002/2013EO450001.
937
938 Wilcock, W. S., Purdy, G. M., & Solomon, S. C. (1990). Microearthquake evidence for
939 extension across the Kane transform fault. Journal of Geophysical Research: Solid Earth,
940 95(B10), 15439-15462. DOI: 10.1029/JB095iB10p15439.
941
942 Yu, Z., Singh, S. C., Gregory, E. P., Maia, M., Wang, Z., & Brunelli, D. (2021). Semibrittle
943 seismic deformation in high-temperature mantle mylonite shear zone along the Romanche
944 transform fault. Science Advances, 7(15), eabf3388. DOI: 10.1126/sciadv.abf3388.
945
946 Yue, H., T. Lay, and K. D. Koper (2012), En échelon and orthogonal fault ruptures of the 11
947 April 2012 great intraplate earthquakes, Nature, 490(7419), 245-249.
948 DOI:10.1038/nature11492.
949

Tables

Tab. 1: PI-LAB network OBS station details. Stations indicated with an asterisk were not used. Except for L27A running time is equivalent to deployment time.

Station	Lon	Lat	Depth (m)	Running Time	Notes
I01D*	-17.8855	1.2734	-4047	N/A	*unrecovered*
L02A	-17.4085	-1.1667	-3499	06/03/2016 – 24/03/2017	*did not level*
S03D	-17.0315	-2.4021	-3750	05/03/2016 – 25/03/2017	
I04D	-16.1733	-2.1238	-3928	07/03/2016 – 24/03/2017	
L05A	-15.4058	-1.8577	-4052	07/03/2016 – 21/03/2017	*stopped after 150 days*
S06D	-14.4298	-1.6703	-3778	06/03/2016 – 19/03/2017	
I07D	-14.0428	-1.5565	-3819	08/03/2016 – 22/03/2017	
L08D*	-13.6409	-1.4493	-3357	08/03/2022 – 18/03/2017	*only 1 horizontal channel*
L09A	-13.3185	-1.3569	-3378	08/03/2016 – 18/03/2017	*1 flat horizontal channel*
S10D	-12.9697	-1.3180	-3015	07/03/2016 – 18/03/2017	
S11D	-12.4602	-1.1691	-2905	07/03/2016 – 18/03/2017	
I12D	-10.7766	-0.8683	-4022	19/03/2016 – 17/03/2017	
L13D	-9.5619	-0.5862	-4659	09/03/2016 – 16/03/2017	*usable data until 23/12/16*
I14D	-7.9524	-0.3522	-4702	10/03/2016 – 10/03/2017	
S15D	-6.6228	0.1814	-4927	09/03/2016 – 16/03/2017	*rocking, some bad data*
L16D	-7.8953	0.8933	-4581	11/03/2016 – 15/03/2017	*usable data until 24/02/16*
S17D	-8.5121	0.7422	-5205	09/03/2016 – 15/03/2017	
L18D	-9.3765	0.5769	-4890	11/03/2016 – 14/03/2017	
S19D	-9.9754	0.4809	-4607	10/03/2016 – 14/03/2017	
I20D	-10.5352	0.3681	-4724	12/03/2016 – 13/03/2017	
L21D	-11.0380	0.2364	-4625	11/03/2016 – 13/03/2017	
S22D	-11.6799	0.1254	-4352	10/03/2016 – 13/03/2017	
L23D*	-12.1478	0.0521	-4631	12/03/2016 – 12/03/2017	*timing issues*
S24D	-12.7806	-0.1383	-4453	10/03/2016 – 13/03/2017	
L25D*	-13.2230	-0.1745	-4207	12/03/2022 – 11/03/2017	*disk failure*
S26D	-13.6260	-0.3434	-4216	11/03/2016 – 12/03/2017	
L27A*	-13.9427	-0.4007	-3928	12/03/2016 – 23/08/2016	*1 flat horizontal channel*
I28D	-14.2684	-0.4918	-3711	13/03/2016 – 11/03/2017	
S29D	-14.6272	-0.5597	-3626	11/03/2016 – 11/03/2017	
L30A	-14.9467	-0.5880	-4003	13/03/2016 – 10/03/2017	
S31D	-15.3188	-0.7141	-3408	11/03/2016 – 11/03/2017	
S32D	-15.6470	-0.7968	-2967	11/03/2016 – 11/03/2017	
L33D	-16.0152	-0.8747	-3919	13/03/2016 – 09/03/2017	
I34D	-16.3485	-0.9579	-2964	14/03/2016 – 09/03/2017	
S35D*	-16.6798	-1.0372	-3773	11/03/2016 – 11/03/2017	*disk failure*
I36D*	-17.0306	-1.1170	-3938	N/A	*unrecovered*
L37D	-14.9718	1.5657	-5054	19/03/2016 – 08/03/2017	
S38D	-12.7623	1.9218	-4926	18/03/2016 – 08/03/2017	
L39D*	-11.4904	2.0557	-4685	20/03/2016 – 07/03/2017	*unrecovered*

Figures

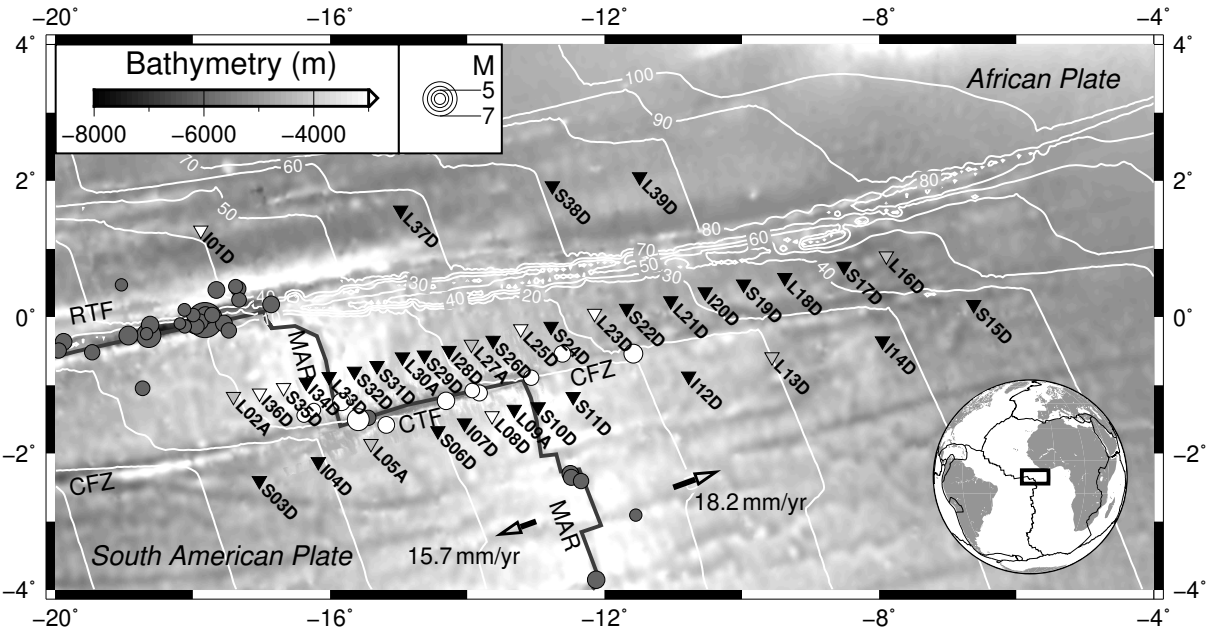

Fig. 1: Map of the study area (see inset for global context), including the PI-LAB station network. Some stations did not provide usable data for the entire timespan of the experiment (white triangles), some stations were only returning useful data for parts of the deployment (grey triangles); see details in Table 1. The thick solid line denotes the locations of the Mid Atlantic Ridge (MAR) and the Romanche and Chain Transform Faults and Fracture Zones (RTF, CTF, CFZ; adapted from Bird, 2003). Events from the ISC during the time of the deployment are shown by circles, events around the CTF and CFZ (white circles) have been used to calibrate the local event magnitude (see Fig. 3). In the global catalogue, all these events have been assigned default depth values of 10km. Bathymetry data is taken from ETOPO1 (Amante & Eakins, 2009) with an additional higher resolution image around the CTF (Harmon et al., 2018). White thin lines show age contours in Ma (Müller et al, 2008). Arrows depict the annual half-spreading rate (Harmon et al., 2018).

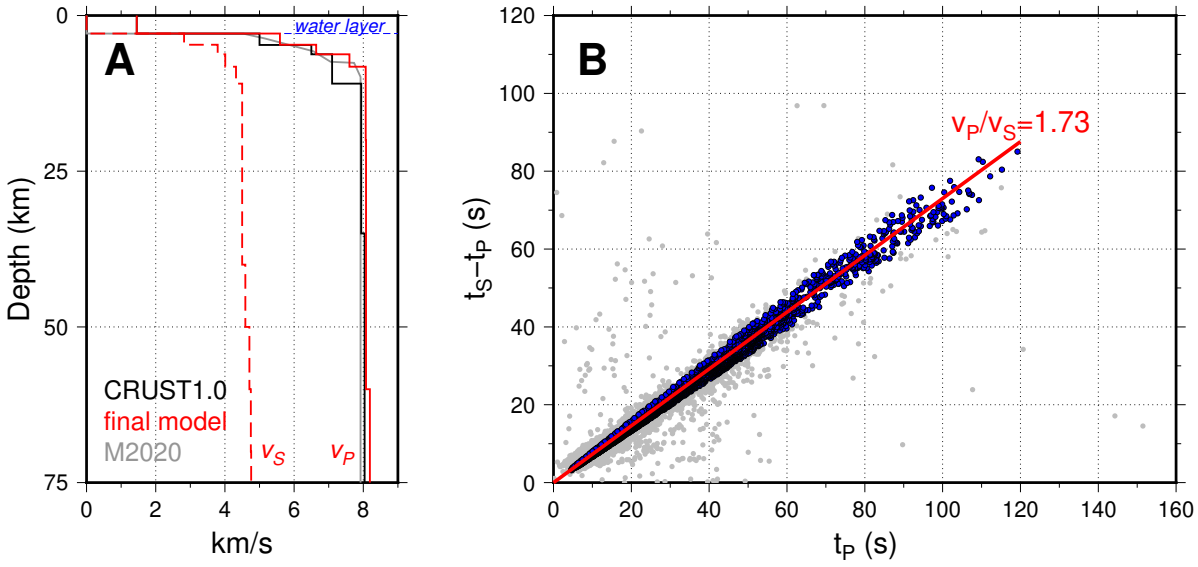

1011

1012 Fig. 2: (A) Initial (CRUST1.0) and final 1-D velocity-depth models. Note that CRUST1.0

1013 only provides a P-velocity model. M2020 shows a model by Marjanovic et al. (2020),

1014 adjusted to the same water column thickness of 2.9 km. (B) Wadati plot of P- and S- arrival

1015 time picks (7345 pairs) for all events. The red line shows the average v_P/v_S ratio of 1.73.

1016 About 97.1% (7130 pairs) fall within ± 0.4 of that value, about 67.0% (4923 pairs in blue)

1017 fall within ± 0.07. See Supplementary Figure S1 for detailed versions of the Wadati plot

1018 divided by station and event origin region.

1019

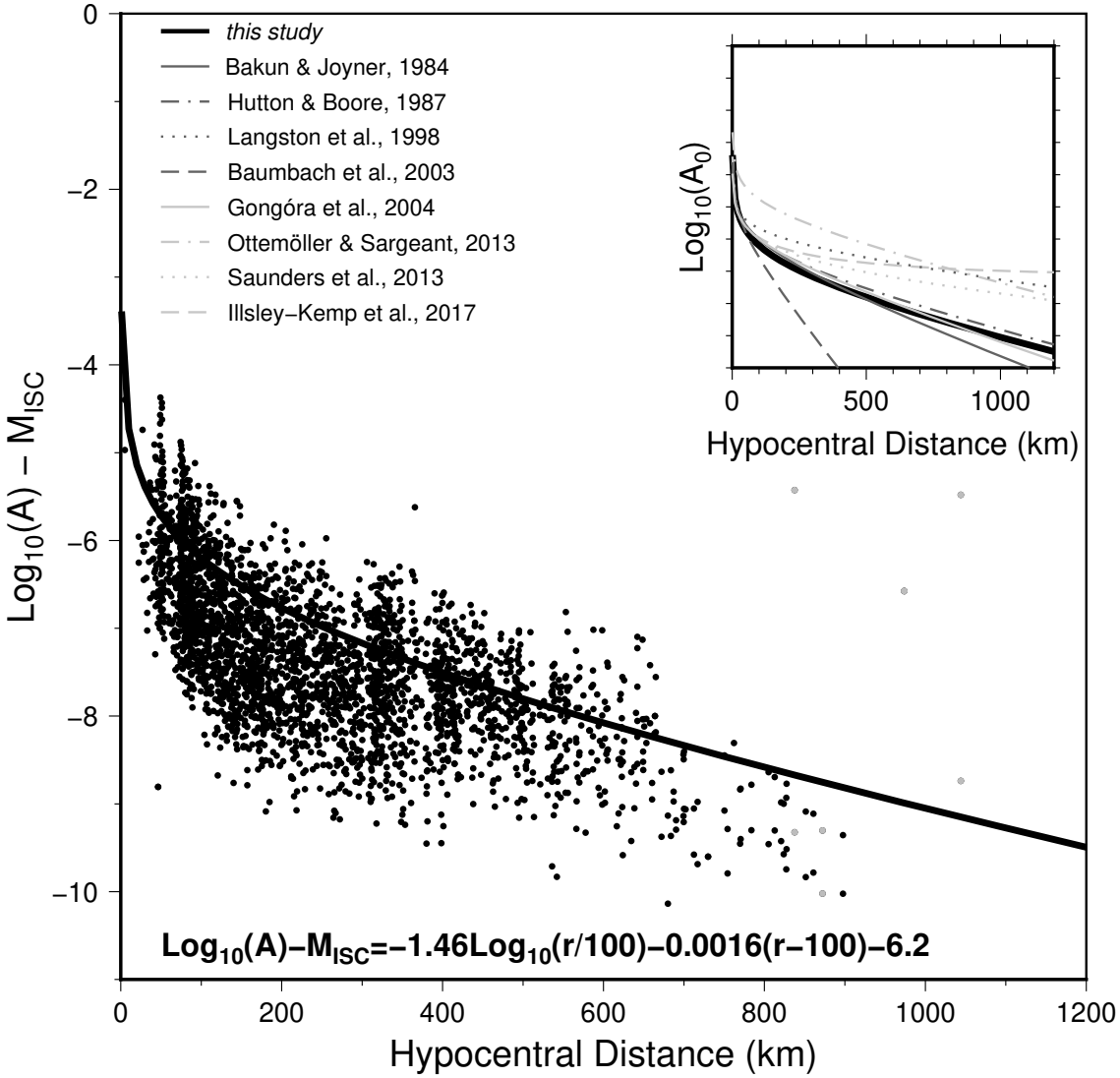

1020

1021 Fig. 3: Magnitude calibration with MT inversion solutions. Note, that results from station
1022 S15D (grey dots) are taken out of the calculation, since the instrument was located on a slope
1023 rocking and produced erroneous data. The inset shows different correction curves, all shifted
1024 to match the original setup by Richter (1935, 1958).

1025

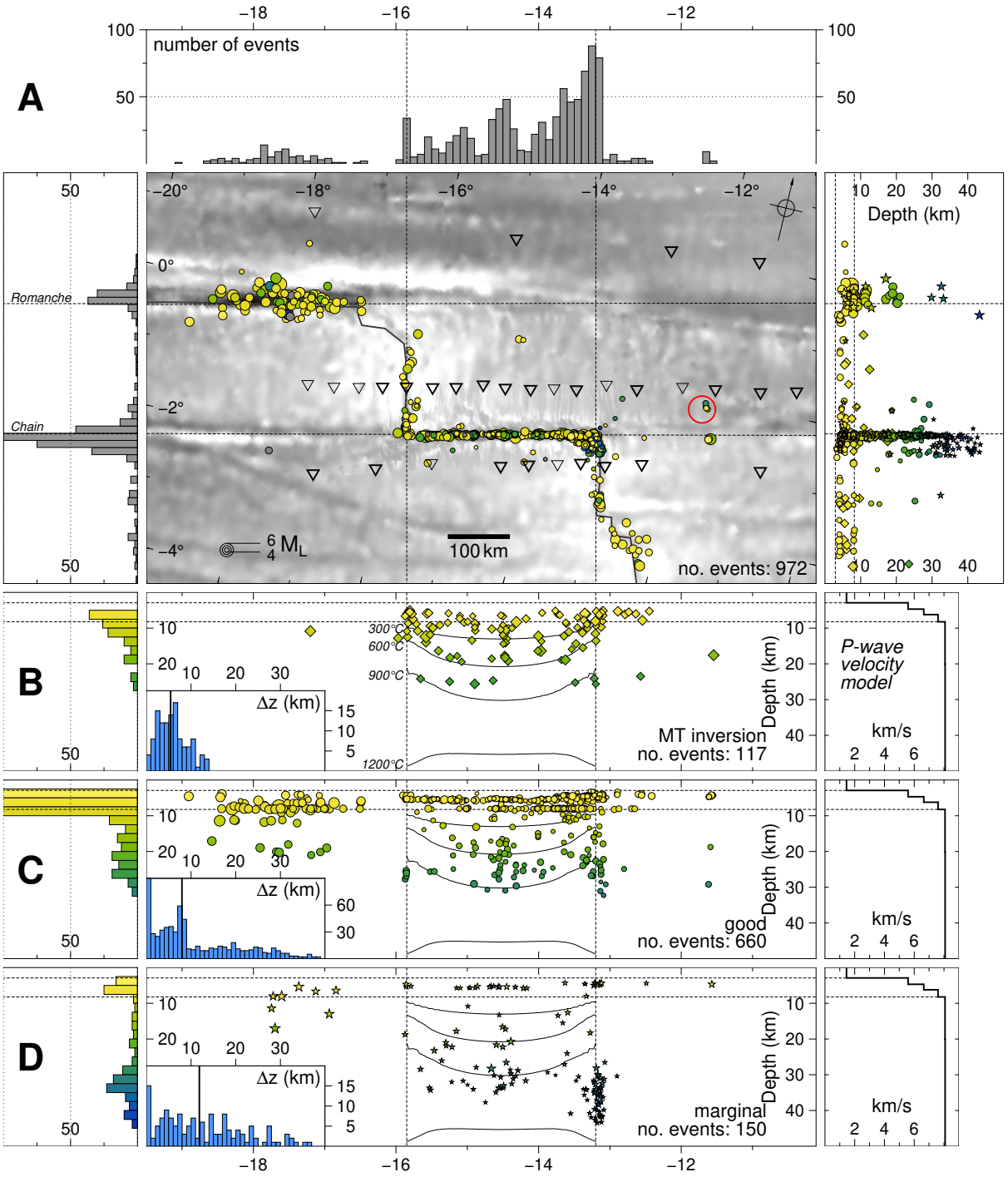

Fig. 4: Catalogue event location and magnitude results. (A) Map showing the epicentres coloured by depth. The red circle indicates the location and rough extent of a high velocity anomaly at 30 km depth (Saikia et al., 2021). Top and left panels show histograms by projected longitude and latitude. The right panel shows a cross section along the MAR, with event symbols representing different result quality levels corresponding to the symbols in the other cross section panels. (B-D) Cross section along the CTF and CFZ. Depth uncertainties

1033 are shown in the blue histograms with the median value being depicted by vertical black
1034 lines. For clarity, error bars have been omitted from the figure but can be seen in
1035 Supplementary Figure S5. Events are divided by quality (B: events for which moment tensor
1036 inversion was possible; C: good locating results with NonLinLoc; D: marginal locating
1037 results with NonLinLoc). Isotherms (300 – 1200˚C in steps of 300˚C) from a half-space
1038 cooling model (using the lower half spreading rate from the African plate, 15.7mm/yr, which
1039 results in deeper isotherms) are also shown along the CTF. Also shown are depth histograms
1040 (left) and the final P-velocity model (right). See Figure 1 for further details. See
1041 Supplementary Table S1 for event details.
1042

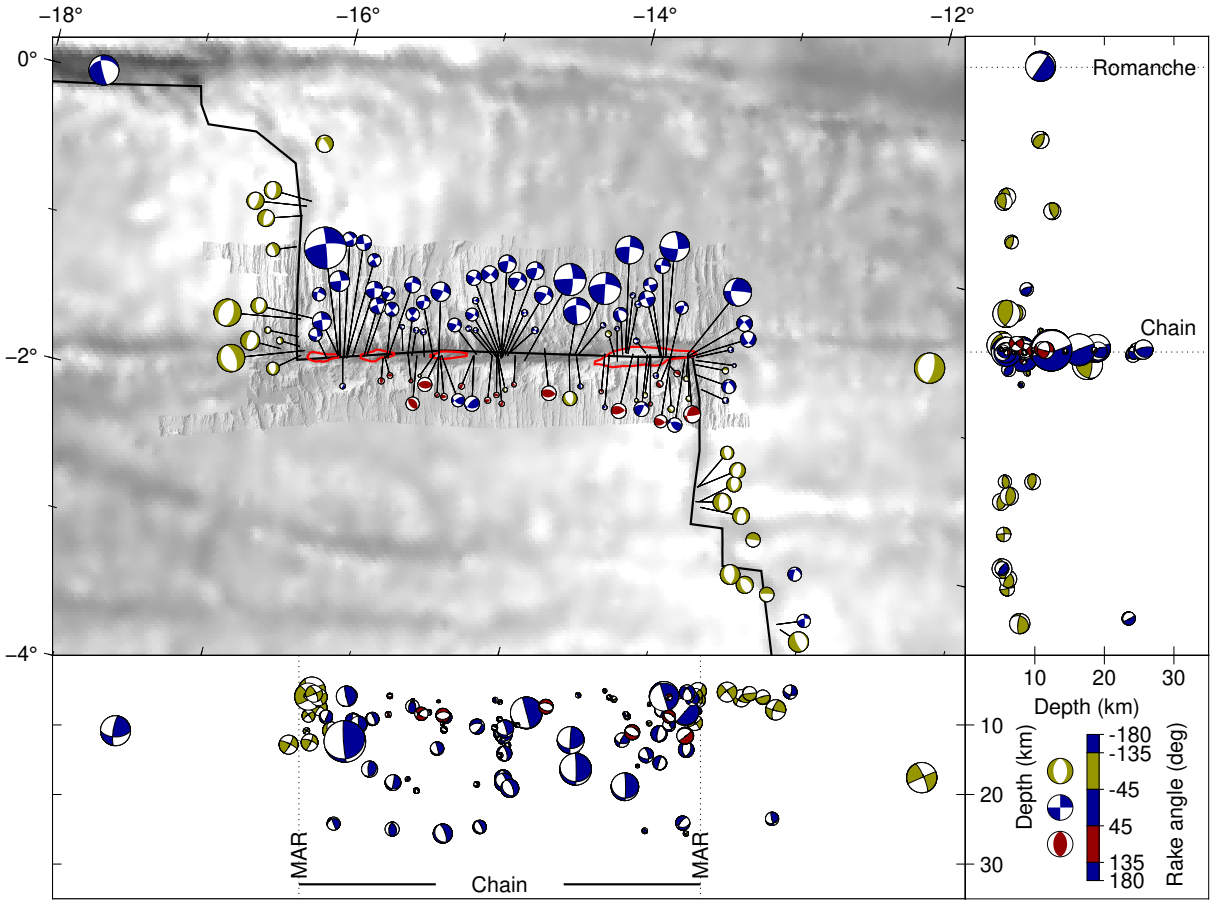

Fig. 5: Map including all focal mechanisms (shown as MT inversion results in Fig. 4). The mechanisms are placed apart from the OTF for better visibility. The shading is based on their dominant mechanism according to rake angle. Red lines indicate mapped transpressive flower-structures on the CTF (Harmon et al., 2018). Zoomed-in views of the regions around the flower structures can be seen in Figure 6. See Figure 1 for further details, Supplementary Table S2 for focal mechanism details, and Supplementary Figure S7 for an example of a waveform fit.

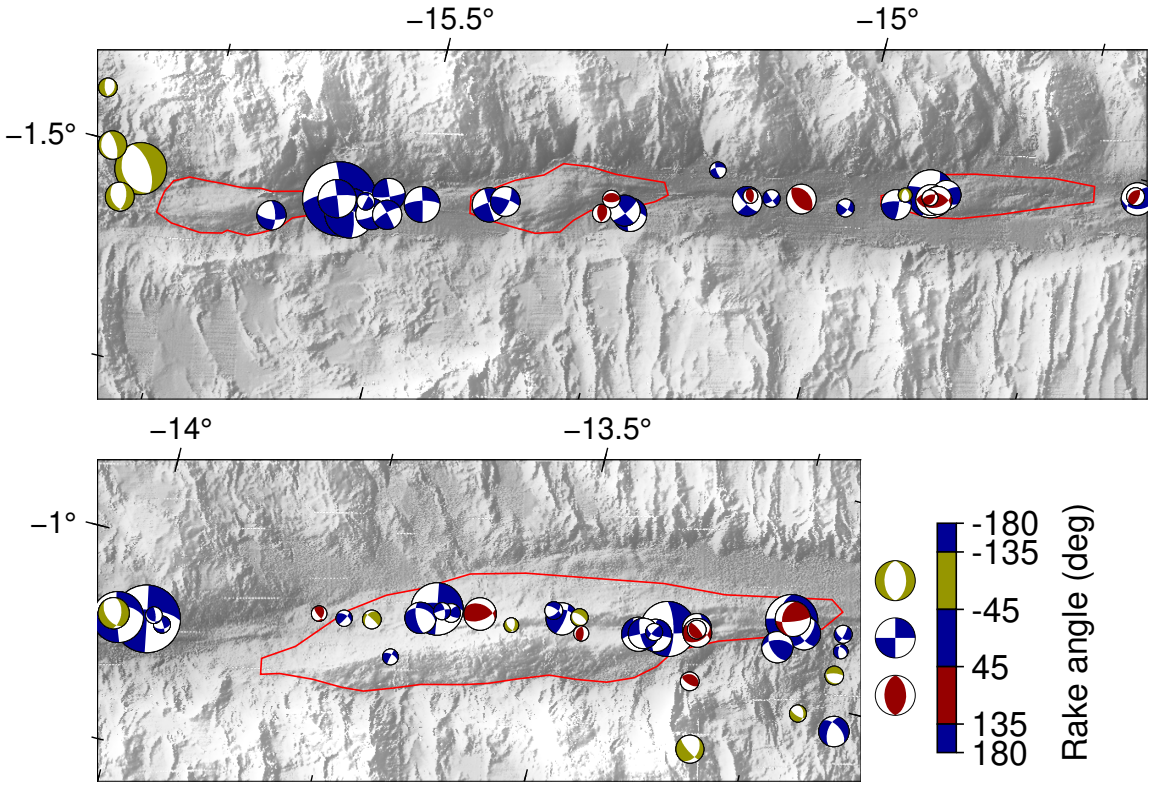

Fig. 6: Zoomed-in versions of flower structures on the CTF, including focal mechanisms, coloured by their rake angle. For further information see Figures 1 and 5.

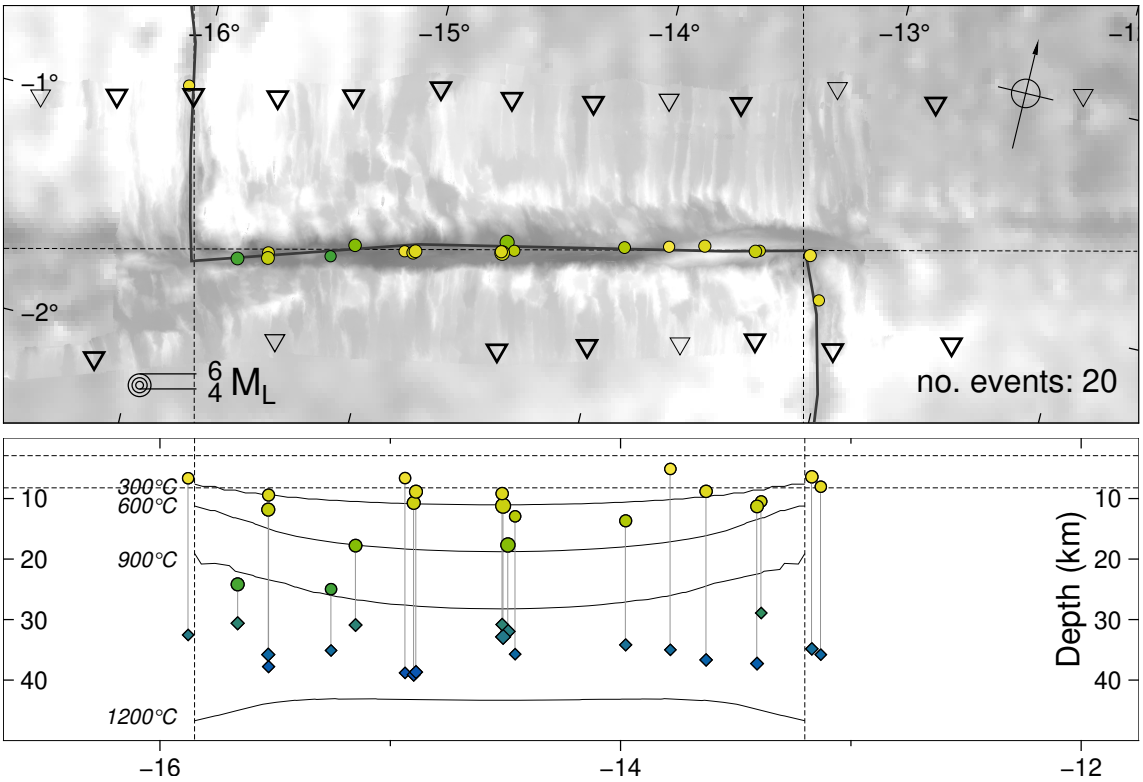

1056

1057 Fig. 7: Map showing all MT results that show a bimodal distribution with good shallow and

1058 deep solutions, including shallow (circles) and deep (diamonds) in the cross section.

1059

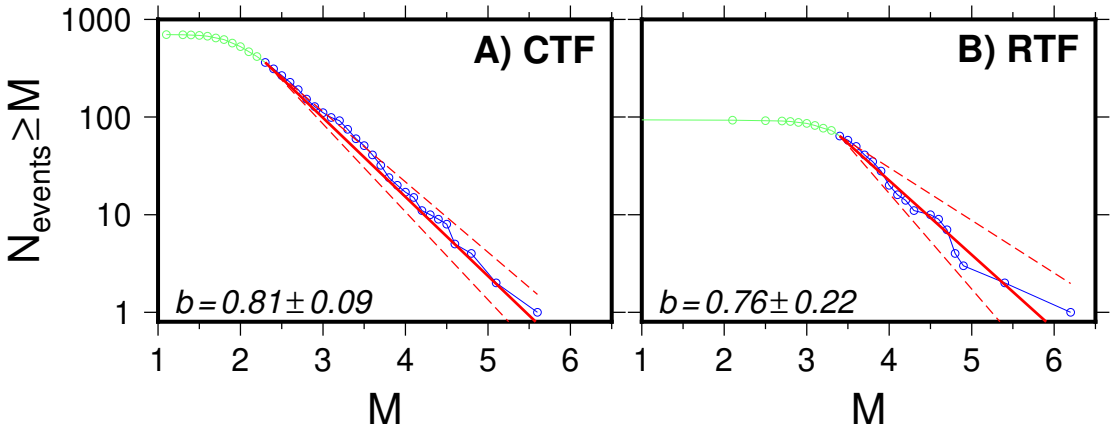

Fig. 8: Earthquake-magnitude distribution on the CTF (A) and RTF (B). Blue circles and lines show the magnitude range used to calculate the Gutenberg-Richter relationship. The result is shown (solid red line) with its uncertainties (dashed red lines).